International Journal of Heat and Mass Transfer 80 (2015) 256–265

Contents lists available at ScienceDirect

International Journal of Heat and Mass Transfer

journal homepage: www.elsevier.com/locate/ijhmt

Heat transfer characteristics and CHF prediction in nanofluid boiling

Jingliang Bi [a,b], Kambiz Vafai [b,*], David M. Christopher [a]

[a] Key Laboratory for Thermal Science and Power Engineering of Ministry of Education, Department of Thermal Engineering, Tsinghua University, Beijing 100084, China
[b] Department of Mechanical Engineering, University of California, Riverside, CA 92521-0425, USA

ARTICLE INFO

Article history:
Received 15 July 2014
Received in revised form 7 September 2014
Accepted 8 September 2014

Keywords:
Nanofluid
Boiling
Average heat flux
CHF
Composite model

ABSTRACT

A composite model for the average heat flux using both pure fluids and nanofluids is established incorporating microlayer evaporation, transient conduction due to bubble departure, and microconvection due to bubble growth and movement. Our model also takes into account bubble influence area interference. The average heat flux and the critical heat flux (CHF) when the surface dryout fraction exceeds a certain value are predicted. Nanofluid properties were calculated and the contact angles obtained from experiments were utilized in the present model. The analytical heat flux and CHF values using both regular fluids and nanofluids were compared with the experimental results and existing theories and were found to be in close agreement. It was found that CHF enhancement value increases to 3.54 as the contact angle decreases from 80° to 20°, which is in agreement with recent experimental results.

1. Introduction

The heat transfer characteristics and thermal properties of nanofluids have been investigated more intensely in the past couple of decades for different heat transfer applications by various researchers [1–3]. Water is the most popular base fluid, while glycol–ethylene, oil, bio-fluids, and polymer solutions have also been used. A variety of materials are commonly used as nanoparticles, such as alumina, titania, silica, zirconia, graphite, carbon nanotubes, diamond, copper and gold. [4]. In addition to single-phase heat transfer applications, nanofluid is also used in two-phase heat transfer applications.

CHF is found to be substantially enhanced with nanofluid boiling, while contradictory results with respect to the average wall heat transfer rates have been reported [5,8–15]. Das et al. [5] experimentally studied pool boiling of alumina-water nanofluid and observed deterioration of the average heat flux. The nanoparticle size range varied from 50 to 150 nm, and the mean diameter was 38 nm. The concentration of the liquid varied from 1% to 4%. They argued that the nanoparticles, which were much smaller than the surface roughness (0.2–1.2 μm), deposit on the relatively uneven surface during boiling and hence created a smoother surface. This causes degradation of the boiling characteristics and the surface smoothening overshadows the thermal conductivity enhancement of the nanofluids. Coursey and Kim [6] employed water and ethanol based nanofluids with aluminum nanoparticle concentrations from 0.001 to 10 g/L. Nanofluids were found to degrade or had little influence on the boiling performance. Larger concentrations ($\geqslant$0.5 g/L) resulted in a moderate (up to 37%) increase in the CHF.

The main reason for the deterioration of heat flux is assumed to be the deposition of nanoparticles on the surface which changes the surface wettability. Kim et al. [7] experimentally studied alumina, silica, and zirconia based nanofluids and found that when the concentration was smaller than 0.1% by volume, CHF could be greatly enhanced due to the buildup of a porous layer of nanoparticles on the surface.

The nanofluid boiling experimental results [5,8–20] are summarized in Table 1. In this Table, nanoparticle size and concentration is specified under the column entitled "nanofluid properties". The heater properties, the contact angle and roughness characteristics are listed under the column entitled "surface property". The average boiling heat flux (BHF), CHF, the boiling heat transfer coefficient (BHTC) as well as the maximum deterioration and enhancement ratios values at specified nanofluid concentrations are also illustrated in Table 1.

Although pool boiling with nanofluids has been investigated extensively experimentally, there are very few reports on an analytical study of nanofluid boiling. Models on nanofluid boiling are needed. Compared to boiling with pure liquid, nanofluid boiling involves the change of liquid thermal properties and the movement of particles. Experiments show that at low concentrations, changes in liquid thermal properties is not significant [12,14,21,22]. Nanoparticles deposited on the surface alter the surface conditions [23] and the surface contact angle [8,11–14]. Surface contact angle is

* Corresponding author.
E-mail address: vafai@engr.ucr.edu (K. Vafai).

http://dx.doi.org/10.1016/j.ijheatmasstransfer.2014.09.019
0017-9310/

Nomenclature

A	Hamaker constant, area
$\overline{A}$	area for each bubble
c	capacity
C_1	empirical constant in Eq. (47)
C_{sf}	coefficient in Eq. (58)
D	bubble diameter
f	bubble departure frequency
F	dryout fraction
Gr	Grashof number
h	heat transfer coefficient
h_{ev}	evaporation coefficient
h_{fg}	latent heat
Ja	Jacob number
k	thermal conductivity
$K_{overlap}$	Enhancement ratio in overlapping area
N_n	active nucleation site density
$\overline{N_n}$	average cavity density
Nu	Nusselt number
N_{sd}	nucleation site density
P	pressure
Pr	Prandtl number
q	heat transfer rate
q''	heat flux
Q	total wall heat transfer
r	radial coordinate
R_0	minimum radius of the microlayer
$R_{\max}$	maximum radius of the microlayer
R_b	bubble radius
R_c	critical cavity radius
Re_b	bubble Reynolds number
R_g	gas constant based on molecular weight
t	time
T	temperature
u	radial velocity
U_b	bubble interface velocity
v	vertical velocity
y	vertical coordinate

Greek symbols

ΔT	temperature difference
β	thermal expansion coefficient
δ	microlayer thickness
θ	surface contact angle
κ	surface curvature
λ'	statistical parameter
μ	dynamic viscosity of the base fluid
ρ	density
ρ^+	non-dimensional density difference
σ	surface tension
φ	heater surface inclination angle
ϕ	nanofluid concentration

Subscripts

0	equilibrium boundary layer
b	bubble
c	contact line
CHF	critical heat flux
d	departure
f	nanofluid
g	growth
int	interface
l	base liquid
max	maximum
mc	microconvection
me	microlayer evaporation
nc	natural convection
$overlap$	overlapping
re	rewetting
R	radius
s	solid nanoparticle
tc	transient conduction
v	vapor
w	wall

an important characteristic and it can substantially influence the active nucleation sites [25]. In our analysis, we will use the contact angle as a parameter to define surface characteristics.

A number of researchers have proposed several theories on the boiling process and the associated heat transfer [26–31]. However, the literature lacks a dominant model representation of boiling heat flux. The earliest researchers simplified the boiling process to a single–phase convection process, including Rohsenow [26], Tien [27] and Zuber [28]. Forster and Greif [29] proposed that departing bubble worked as a micropump to push hot liquid away and cold liquid in. Mikic and Rohsenow [31] postulated that when bubbles depart, they take away the superheated liquid layer adjacent to the heating surface and cold liquid rushes in and transient conduction occurs.

Different mechanisms are active during different bubble periods. Judd and Huang [32] first combined microlayer evaporation, transient conduction and natural convection to set up a comprehensive model for boiling heat transfer. Benjamin and Balakrishnan [33] proposed a similar model and accounted for the activation period for transient conduction and microlayer evaporation. These two models considered the situations at low to moderate heat flux regions where bubbles did not interfere with each other. Since the boiling heat transfer attributes has not been fully understood, more work needs to be done to better reveal the heat transfer mechanism in nucleate boiling.

Critical heat flux (CHF) is also an important characteristic in boiling. CHF is the end of nucleate boiling and refers to the limit of safe operation of a heat transfer system. In nuclear reactors or electrical components, loss of liquid contact with surface will dramatically decrease the heat transfer coefficient and causes damage to the surfaces. To investigate CHF and its mechanism, a number of theories have been proposed to predict the critical heat flux.

Zuber [34] proposed that Taylor and Helmholtz instabilities were responsible for the occurrence of CHF. As the heat flux increases, the velocity of vapor jets above the nucleating bubbles increase dramatically, occupying the space of liquid between the jets toward the surface thus initiating an instability process. Zuber's correlation is the most widely used to predict pool boiling CHF as:

$$q_{\mathrm{CHF}} = 0.131\rho_v^{0.5}h_{fg}\left[\sigma g\left(\rho_f - \rho_v\right)\right]^{0.25} \tag{1}$$

Haramura and Katto [35] proposed a hydrodynamic model, that is, as the heat flux exceeds a certain value, a vapor blanket forms on the liquid film preventing bulk liquid from feeding the film resulting in the dryout of the liquid film thus substantially enhancing occurrence of CHF.

Kandlikar [36] took the effect of dynamic receding contact angle into consideration and developed a theoretical model to predict the CHF in saturated pool boiling. As the surface heat flux

Table 1
Synthesis of the pertinent nanofluid boiling experiments in the last decade.

References	Nanofluid properties	Surface property	CHF	Average boiling heat flux
Shahmoradi et al. [8]	Al_2O_3 (40 nm)–water (0.001–0.1 vol.%)	Flat plate heater (θ from 45° to 20°) (*Ra* from 5.1 nm to 376 nm; 77 nm to 197 nm)	CHF ↑ 47% for 0.1 vol.%	BHF ↓ 40% for 0.1 vol.%
Jung et al. [9]	Al_2O_3 (46 nm) + H_2O/LiBr (0.01–0.1 vol%)	Plate copper heater (θ from 78° ↓ to 36°)	CHF ↑ by 48.5% at 0.1 vol.%	BHF ↓ 10%
Vazquez and Kumar [10]	Silica (10 nm)–water 0.1 to 2 vol.%	Nichrome wires and ribbons	CHF ↑ 270% at 0.4 vol.%	BHF ↑ 190%
Jung et al. [11]	Al_2O_3 (45 nm)–water (10^{-5}–0.1 vol.%).	Plate copper heater	CHF ↑ 116%	BHF ↓ 60%
Hegde et al. [12]	CuO (50 nm)–water, (0.01–0.5%)	NiCr wire (from 0.34 μm to 0.09 (0.05 vol.%) and 0.23 μm (0.3%))	CHF ↑ 130% (1.3–3 MW/m^2)	BHF ↓ 50%
Kole and Dey [13]	ZnO (30–40 nm)–ethylene glycol (EG)	Copper cylindrical block (90 nm)	CHF ↑ by 117% at 2.6%	BHF ↑ by 22% at 1.6% and ↓ further loading
Bolukbasi and Ciloglu [14]	SiO_2 (34 nm)–water (0.001–0.1 vol.%)	Cylindrical brass (typical 90 nm) (*Ra* ↑ to 620 nm, θ70° to 42.07° and 9.97°)	CHF ↑ 28%	BHF ↓ 40%
Gerardi et al. [15]	Diamond (34 nm) and silica–water (173 nm) (0.1 vol.% for silica and 0.01 vol.% for diamond)	Upward indium-tin-oxide surface (θ from 80° to 16°) (*Ra* from 30 to 900–2100 nm)	CHF ↑ 100%	BHTC ↓ 50%
Wen et al. [16]	Al_2O_3 (50–900 nm)–water (0.001–0.1%)	Rectangular brass plates (rough: 420 nm and smooth: 25 nm)	–	Two-fold ↑ in BHTC at 0.001% nanofluids
Suriyawong and Wongwises. [17]	TiO_2–water (21 nm), 0.00005–0.01 vol.%	Horizontal circular plates, copper (*Ra* 0.2 μm) and aluminium (*Ra* 4 μm)	–	BHTC 15% ↑ for copper and a 4% ↑ for aluminium at 0.0001 vol.%; ↓ at higher conc levels
Kwark et al. [18]	(Al_2O_3, CuO and diamond)–water (2.7×10^{-5}–2.7×10^{-2}% vol.).	1 cm × 1 cm × 0.3 cm copper block	CHF ↑ 31%	BHF no change <500 KW/m^{2}and ↓ at high heat flux
Liu et al. [19]	CuO (30 nm)–water	Copper block	CHF ↑ when conc <1%; constant since	BHF ↑ when conc <1%; ↓ >1%
You et al. [20]	Al_2O_3–water (0–0.05 g/l)	Polished copper surfaces	CHF ↑ 200%	Same
Das et al. [5]	Al_2O_3 (50–150 nm)–water (1–4%)	Rectangular stainless steel (0.4 and 1.15 μm)	–	BHF ↓

increases, the force resulting from the evaporation at the bubble interface exceeds the gravitational and surface tension forces that are holding the bubble, resulting in the spread of vapor bubble over the surface causing CHF to occur. The following correlation by Kandlikar [36] predicts the effect of surface orientation angle and system pressure on CHF:

$$q''_{CHF} = \rho_v^{\frac{1}{2}} h_{fg} \left(\frac{1+\cos\theta}{16}\right) \times \left[\frac{2}{\pi} + \frac{\pi}{4}(1+\cos\theta)\cos\varphi\right]^{\frac{1}{2}} \left[g\sigma(\rho_f - \rho_v)\right]^{\frac{1}{4}} \quad (2)$$

where θ is the receding contact angle and φ is the heater surface angle. The above equation predicts a continuous increase of CHF with decreasing surface contact angle.

The present work incorporates the main mechanisms in the boiling process and extends the analysis to high heat flux region where bubble influence areas interfere with each other. The CHF value can also be predicted by the present model. The obtained analytical results were compared with recent experimental results and classical equations and were found to be in good agreement.

2. Nanofluid properties

The density of a nanofluid can be expressed based on the mixture rule as:

$$\rho_f = (1-\phi)\rho_l + \phi\rho_s \quad (3)$$

Similarly, specific heat and thermal expansion coefficient of nanofluid can be expressed [37] as:

$$c_f = \frac{(1-\phi)\rho_l c_l + \phi\rho_s c_s}{\rho_f} \quad (4)$$

$$\beta_f = \frac{(1-\phi)(\rho_l\beta_l) + \phi\rho_s\beta_s}{\rho_f} \quad (5)$$

The dynamic viscosity can be expressed as [38]:

$$\mu_f = (1 + 2.5\phi + 6.2\phi^2)\mu_l \quad (6)$$

and the thermal conductivity can be expressed based on the correlation proposed by Khanafer and Vafai [37]:

$$k_f = k_l\left[1.0 + 1.0112\phi + 2.4375\phi\left(\frac{47}{d_s(\text{nm})}\right) - 0.0248\phi\left(\frac{k_s}{0.613}\right)\right] \quad (7)$$

3. Model development

Boiling is a complex phenomenon as it involves both phase change and forced convection due to bubble movement. A number of researchers have divided the analysis of pool boiling heat transfer into different parts [32,33]. In prior works, microlayer evaporation and transient conduction during bubble waiting time were analyzed in detail. However microconvection has not received much attention. In the present work, the total heat flux is divided into 4 parts: Microlayer evaporation, transient conduction under bubble, transient conduction after bubble departs, and enhanced natural convection. The interference of bubble influence areas was also analyzed in the present work.

3.1. Total bubble heat transfer in one bubble ebullition cycle

3.1.1. Microlayer evaporation

Microlayer evaporation is considered to be an important mechanism during the bubble growth phase. The evaporation of this thin liquid layer under the bubble generates the vapor needed for the bubble growth as shown in Fig. 1a. However, due to the very small size of the microlayer, it is difficult to directly observe and measure it. An analytical model is presented here to predict the microlayer shape and the heat transfer rate. The microlayer is considered within a cylindrical coordinate system. The continuity equation for the microlayer can be expressed as:

$$\frac{1}{r}\frac{\partial}{\partial r}(ru_f) + \frac{\partial v_f}{\partial y} = 0 \quad (8)$$

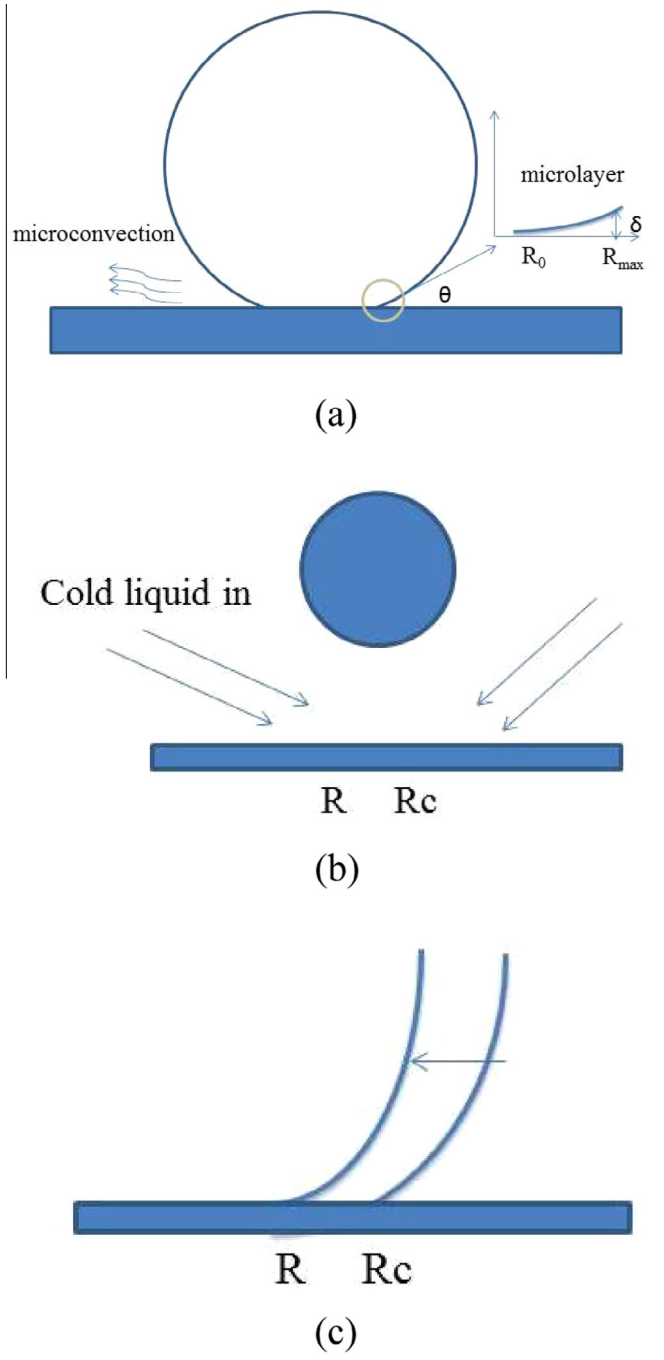

Fig. 1. illustration of (a) microlayer and microconvection, (b) liquid rewetting surface after bubble departure, (c) transient conduction before bubble departure.

The radial momentum equation in the microlayer assumes the advection term is negligible and that the velocity gradient in the radial direction is much smaller than the velocity gradient in the vertical direction, so the lubrication approximation can be invoked to arrive at:

$$\frac{\partial P_f}{\partial r} = \mu_f \frac{\partial^2 u_f}{\partial y^2} \tag{9}$$

The velocity at $y = 0$ and the shear stress at the interface is zero, so the boundary conditions can be expressed as:

$$u_f(y=0) = 0, \quad \frac{\partial u_f}{\partial y}(\delta) = 0 \tag{10}$$

Integrating Eq. (9) subject to the boundary conditions in Eq. (10), results in the following expression for the velocity along the microlayer:

$$u_f = -\frac{1}{\mu_f}\frac{\partial P_f}{\partial r}\left(\delta y - \frac{y^2}{2}\right) \tag{11}$$

Integrating Eq. (8) and solving for v_f gives:

$$v_f(\delta) - 0 = -\frac{1}{r}\frac{\partial}{\partial r} r \int_0^{\delta} u_f dy \tag{12}$$

Substituting Eq. (11) in Eq. (12), the vertical velocity can be expressed as:

$$v_f(\delta) = \frac{\delta^3}{3r\mu_f}\frac{\partial}{\partial r}\left(r\frac{\partial P_f}{\partial r}\right) \tag{13}$$

Since the microlayer is quite thin, the velocity due to bubble evaporation perpendicular to the bubble interface is essentially vertical:

$$v_f(\delta) = \frac{q''}{\rho_f h_{fg}} \tag{14}$$

Eqs. (13) and (14) can be combined and rearranged as:

$$\frac{3r\mu_f q''}{\rho_f h_{fg}\delta^3} = \frac{d}{dr}\left(r\frac{dP_f}{dr}\right) = \frac{dP_f}{dr} + r\frac{d^2P_f}{dr^2} \tag{15}$$

The heat flux through the microlayer is based on Fourier's law,

$$q'' = k_f \frac{(T_w - T_{\text{int}})}{\delta} \tag{16}$$

While the modified Clausius–Clapeyron equation [39] for the heat transfer across the interface can be written as:

$$q'' = h_{ev}\left[T_{\text{int}} - T_v + \frac{(P_f - P_v)T_v}{\rho_v h_{fg}}\right] \tag{17}$$

As such, the interface temperature T_{int} can be obtained by combining Eqs. (16) and (17) as:

$$\left(\frac{k_f}{\delta} + h_{ev}\right)T_{\text{int}} = \left[\frac{k_f}{\delta}T_w + h_{ev}T_v - h_{ev}\frac{(P_f - P_v)T_v}{\rho_v h_{fg}}\right] \tag{18}$$

Pressure drop across the interface is given by the modified Young–Laplace's equation, obtained by a force balance which includes the surface tension, disjoining pressure, and the vapor recoil force:

$$P_f = P_v - \sigma\kappa - \frac{A}{\delta^3} + \frac{q''^2}{\rho_v h_{fg}^2} \tag{19}$$

where A is the Hamaker constant and is chosen as 10^{-21} based on neglecting the recoil pressure term in Eq. (19). This results

$$P_f = P_v - \sigma\kappa - \frac{A}{\delta^3} \tag{20}$$

In the dryout region, $q'' = 0$ and $T_{\text{int}} = T_w$. Substituting for a zero curvature and heat flux in the above equation, the thickness of the dryout area is found to be:

$$\delta_0^3 = \frac{A}{\left(\frac{T_{\text{int}}}{T_v} - 1\right)h_{fg}\rho_v} \tag{21}$$

The interfacial curvature is calculated as:

$$\kappa = \frac{1}{r}\frac{\partial}{\partial r}\left[\frac{r\frac{\partial\delta}{\partial r}}{\sqrt{1 + \left(\frac{\partial\delta}{\partial r}\right)^2}}\right] \tag{22}$$

Calculating the derivative of P_f in Eq. (19) results

$$\frac{dP_f}{dr} = -\sigma\kappa' + 3\frac{A}{\delta^4}\delta' \tag{23}$$

and the second derivative is also calculated to be:

$$\frac{d^2P_f}{dr^2} = -\sigma\kappa'' + 3\frac{A}{\delta^4}\delta'' - 12\frac{A}{\delta^5}\delta'^2 \tag{24}$$

Combining Eqs. (15), (23) and (24) to replace the first and second derivatives of P_f, results in an expression for the second derivative of the curvature:

$$F_1(\delta) = \kappa'' = \left(-\frac{3\mu_l q''}{\rho_f h_{fg}\delta^3} - \frac{\sigma\kappa'}{r} + 3\frac{A}{r\delta^4}\delta' + 3\frac{A}{\delta^4}\delta'' - 12\frac{A}{\delta^5}\delta'^2\right)\Big/\sigma \tag{25}$$

Calculating the second derivative of κ from Eq. (22) results:

$$\begin{aligned}\frac{d^2\kappa}{dr^2} &= \frac{2\delta'}{r^3\left(1+\delta'^2\right)^{\frac{1}{2}}} + \frac{r\delta''' - 2\delta''}{r^2\left(1+\delta'^2\right)^{\frac{3}{2}}} - \frac{3\delta'\delta''^2 + 3r\delta''^3 + 9r\delta'\delta''\delta'''}{r\left(1+\delta'^2\right)^{\frac{5}{2}}} \\ &\quad + \frac{15\delta'^2\delta''^3}{\left(1+\delta'^2\right)^{\frac{7}{2}}} + \frac{\delta''''}{\left(1+\delta'^2\right)^{\frac{3}{2}}} \\ &= F_2(\delta) + \frac{\delta''''}{\left(1+\delta'^2\right)^{\frac{3}{2}}}\end{aligned} \tag{26}$$

Combining Eqs. (25) and (26), the fourth derivative of δ can be obtained as:

$$\delta'''' = [F_1(\delta) - F_2(\delta)]\left(1+\delta'^2\right)^{\frac{3}{2}} \tag{27}$$

The slope of the microlayer at $R_{\max}$ is $\tan(\theta)$ and the radius of the outer edge of the microlayer is $R\sin\theta$ hence the boundary conditions at the microlayer can be presented as:

$$\delta(R_0) = \delta_0, \quad \delta'(R_0) = 0$$

$$\delta'(R_{\max}) = \tan(\theta), \quad R_{\max} = \frac{D}{2}\sin(\theta) \tag{28}$$

3.1.2. Transient conduction after bubble departs

Experiments have shown that the transient conduction is the dominant heat transfer mode in nucleate pool boiling [40,41]. Mikic and Rohsenow [31] were the first to propose a model and provide an expression representing transient conduction during the bubble waiting time. Their model assumes that when a bubble departs from the surface, it carries away the liquid with a radius of a bubble departure diameter, while the cold liquid rushes towards the surface. This process is illustrated in Fig. 1b. The heat transfer from the heating surface to the bulk liquid is considered as transient conduction from a hot surface to a semi-infinite body, which is the bulk liquid in this case.

The instantaneous heat flux at any time is expressed as:

$$q''_{tc}(t) = \frac{k_f\Delta T}{\sqrt{\pi\alpha t}} \tag{29}$$

In this work, the transient conduction t_{tc}, is taken to be three times that of the growth time t_g [33]. Integrating Eq. (29) over the time period t_{tc} and an influence area of four times the bubble projecting area as suggested by various researchers [31–33], the total heat transfer during the waiting period at low heat flux region can be obtained as:

$$Q_{tc} = \int_0^{\frac{3}{4f}} q''_{tc}dt\cdot\pi D^2 = \int_0^{\frac{3}{4f}} \frac{k_f\Delta T}{\sqrt{\pi\alpha t}}dt\cdot\pi D^2 = \frac{\sqrt{3}\pi k_f\Delta T D^2}{\sqrt{\pi\alpha f}} \tag{30}$$

Eq. (30) is valid only when the influence areas do not interfere with each other. To take into account the bubble influence area interference, a dryout fraction parameter F is defined as the ratio of bubble projecting area to the entire heating surface as:

$$F = \frac{\pi}{4}D_d^2 N_{sd} \tag{31}$$

When $\pi D_d^2 \leqslant 1/N_{sd}$, the bubble influence area is smaller than the average area for each bubble on the heating surface and the bubble interfaces are considered not to overlap. For this condition, the dryout fraction F is less than 25% according to Eq. (31). When the dryout fraction exceeds 25%, the influence areas will be overlapping. The overlapping area is a function of the nucleation site density and the bubble influence area. The total overlapping area over the heating surface within a unit area (1 m^2) is:

$$\overline{A}_{total} = \pi D_d^2\cdot N_{sd} - 1 \tag{32}$$

For each bubble, the average overlapping area can be approximated as the total overlapping area divided by the number of active nucleation sites in one unit area. Since each overlapping area is shared by two interfering bubbles, the average overlapping area for each bubble can be represented as:

$$\overline{A}_{overlap} = \frac{1}{2}\left(\pi D_d^2 - 1/N_{sd}\right) \tag{33}$$

Therefore, the non-overlapping area for each bubble is:

$$\overline{A}_{non-overlap} = 1/N_{sd} - \frac{1}{2}\left(\pi D_d^2 - 1/N_{sd}\right) = 3/2N_{sd} - \frac{1}{2}\pi D_d^2 \tag{34}$$

The effect of overlapping of more than three bubbles was considered to be balanced by a heat transfer augmentation of the overlapping area due to repeated quenching.

In the overlapping area, due to repeated quenching, the transient conduction heat flux is larger than the heat flux at non-overlapping areas. This enhancement ratio was determined by considering the two interfering bubble influence areas, with each bubble departing and entering during the waiting period. The enhancement ratio is defined as:

$$K_{overlap} = \frac{\int_0^{\frac{3}{4f}} q''_{tc}dt + \int_0^{\frac{1}{4f}} q''_{tc}dt}{\int_0^{\frac{3}{4f}} q''_{tc}dt} = \frac{\sqrt{3}+1}{\sqrt{3}} = 1.58 \tag{35}$$

So in the high heat flux region, the total heat transfer after bubble departs from the surface is

$$\begin{aligned}Q_{tc} &= \frac{\sqrt{3}k_f\Delta T}{\sqrt{\pi\alpha f}}\left(K_{overlap}\cdot\overline{A}_{overlap} + \overline{A}_{non-overlap}\right) \\ &= \frac{\sqrt{3}k_f\Delta T}{\sqrt{\pi\alpha f}}\left(\frac{K_{overlap}}{2}\left(\pi D^2 - \frac{1}{N_{sd}}\right) + \left(\frac{3}{2N_{sd}} - \frac{\pi D^2}{2}\right)\right)\end{aligned} \tag{36}$$

3.1.3. Transient conduction before the bubble departs

This mode of heat transfer occurs when the bubble contact line starts to shrink and the surface under the bubble is rewetted. The enhanced heat flux has been observed by various researchers [42–45]. The bubble starts to recede from R_c, which is the radius of the contact line. The rewetting process ends when the radius diminishes to zero as the bubble departs. The rewetting process before bubble departure is illustrated in Fig. 1c.

Considering when the liquid front approaches R from R_c ($0 \leqslant R \leqslant R_c$), the heat transfer rate at time t_R in this rewetting process can be obtained by integrating the heat flux from the contact line to where the liquid front is encountered, resulting in

$$q(t_R) = \int_{R_c}^{R} \frac{k_f\Delta T}{\sqrt{\pi\alpha}}\frac{2\pi r dr}{\sqrt{t_R - t_r}} \tag{37}$$

Assuming the bubble contact line receding velocity, u_c, is constant, the total rewetting time is $t_{re} = R_c/u_c$, and the time when the contact line approaches R is $t_R = (R_c - R)/u_c$. Substituting t_R and t_{re} into Eq. (37), the heat transfer rate at the moment t_R is obtained as:

$$q(t_R) = \frac{4\pi k_f \Delta T u_c}{\sqrt{\pi\alpha}}\left(R_c t_R^{1/2} - \frac{2}{3}u_c t_R^{3/2}\right) \tag{38}$$

Integrating the heat transfer rate over the time period t_{re}, the total heat transfer during the bubble rewetting period can be represented as:

$$Q_{re} = \int_0^{t_{re}} q_{re}(t) = \frac{8\pi k_f \Delta T u_c}{3\sqrt{\pi\alpha}}\left(R_c t_{re}^{3/2} - \frac{2}{5}u_c t_{re}^{5/2}\right) \tag{39}$$

The radius of the contact can be written as $R_c = D/2\sin(\theta)$. The rewetting time t_{re} is about half of the growth time t_g [43], and $t_w = 3t_g$ is often considered in the nucleate boiling case [33], so $t_{re} = 1/8f$. Substituting t_{re} into Eq. (39), the heat transfer during the rewetting period can be expressed as:

$$Q_{re} = \frac{8k_f \Delta T R_c^2}{5\sqrt{\alpha}} t_{re}\sqrt{\pi f} = 0.05\frac{k_f \Delta T D_d^2 \sin^2\theta}{\sqrt{\alpha f}}\sqrt{\pi} \tag{40}$$

3.1.4. Microconvection and natural convection

The natural convection heat transfer coefficient over a horizontal flat plate can be expressed as:

$$Nu = 0.31(Gr\cdot \mathrm{Pr})^{1/3} \tag{41}$$

$$q''_{nc} = h\cdot\Delta T = \frac{Nu\cdot k_f}{d}\Delta T \tag{42}$$

$$Q_{nc} = q''_{nc}\left(1/N_{sd} - \pi D_d^2\right) \Big/ f = \frac{0.31(Gr\cdot\mathrm{Pr})^{1/3}\cdot k_f\left(1/N_{sd} - \pi D_d^2\right)}{df}\Delta T \tag{43}$$

In nucleate boiling, the rapid bubble growth perturbs the liquid and enhances the natural convection. In addition to the bubble growth perturbing the liquid slightly, bubbles can also oscillate slightly during the bubble growth period. The natural convection is enhanced due to bubble growth, oscillation and departure. This part of enhanced convection around the bubble is referred to as microconvection and to evaluate its effect we utilize the local Nusselt number expression for forced convection over a flat plate.

The Reynolds number was calculated using Forster and Zuber's definition [46] as:

$$\mathrm{Re}_b = \frac{\rho_v U_b D}{\mu_f} \tag{44}$$

The bubble growth velocity can be written as:

$$R_b = Ja\left(\frac{\alpha t}{\pi}\right)^{1/2}, \quad U_b = dR_b/dt \tag{45}$$

where $Ja = \rho_f c_f(T_w - T_{sat})/(\rho_v h_{fg})$. Substituting Eq. (45) in Eq. (44), the Reynolds number can be represented as:

$$\mathrm{Re}_b = \frac{\rho_f}{\mu_f}\left(\frac{\Delta T C_f \rho_f \sqrt{\alpha}}{h_{lv}\rho_v\sqrt{\pi}}\right)^2 \tag{46}$$

The Nusselt number due to microconvection is expressed based on laminar flow over a flat plate by

$$Nu_{mc} = C_1 \mathrm{Re}_b^m (\mathrm{Pr})^{1/3} \tag{47}$$

where C_1 is 0.332 as is the case for the forced convection over a flat plate, and m is 0.67 as in Rohsenow's model [26].

For the low heat flux region, where bubble influence areas do not interfere with each other, the total area of the microconvection is considered to be within the influence area and outside the bubble contact area and the total time t_g, is 1/4 of the total ebullition cycle. As such, the microconvection can be expressed as:

$$Q_{mc} = \frac{0.332\mathrm{Re}_b^{0.67}(\mathrm{Pr})^{1/3}\cdot k_f}{4f\cdot D_d}\Delta T\left(\pi D_d^2 - \frac{\pi D_d^2\sin^2\theta}{4}\right) \tag{48}$$

If the nucleation site density is too large, the bubble influence areas will interfere with each other. Considering the overlapping area will be influenced by two independent bubbles, microconvection over this area will be repeated, hence the enhancement ratio can be considered to be doubled. As such the total microconvection can be expressed as:

$$q''_{mc} = \frac{Nu_{mc}\cdot k_f}{D_d}\Delta T \tag{49}$$

$$\begin{aligned} Q_{mc} &= \frac{1}{4f}\left(2q''_{mc}\overline{A}_{overlap} + q''_{mc}\left(\overline{A}_{non-overlap} - \frac{\pi D_d^2\sin^2\theta}{4}\right)\right) \\ &= \frac{0.332\mathrm{Re}_b^{0.67}(\mathrm{Pr})^{1/3}\cdot k_f}{8fD_d}\Delta T\left(\pi D_d^2 + \frac{1}{N_{sd}} - \frac{\pi D_d^2\sin^2\theta}{2}\right) \end{aligned} \tag{50}$$

3.2. Nucleation site density

The active nucleation sites N_{sd} can be predicted using Hibiki and Ishii's equation [47].

$$N_n = \overline{N_n}\left\{1 - \exp\left(-\frac{\theta^2}{8\mu^2}\right)\right\}\left[\exp\left\{f(\rho^+)\frac{\lambda'}{R_c}\right\} - 1\right] \tag{51}$$

where
$\overline{N_n} = 4.72\times10^5$ sites/m^2, $\mu = 0.722$ rad, and $\lambda' = 2.50\times10^{-6}$ m,

$$R_c = \frac{2\sigma\left\{1 + (\rho_g/\rho_f)\right\}/P_f}{\exp\left\{h_{fg}(T_g - T_{sat})/(R_g T_g T_{sat})\right\} - 1} \tag{52}$$

$$\begin{aligned} f(\rho^+) = {} & -0.01064 + 0.48246\rho^+ - 0.22712\rho^{+2} \\ & + 0.05468\rho^{+3} \end{aligned} \tag{53}$$

and $\rho^* = \Delta\rho/\rho_g$, $\rho^+ = \log(\rho^*)$ and R_g is the gas constant based on the molecular weight. This correlation predicts a decrease in active nucleation sites with a decrease in the contact angle. In nanofluid boiling, the nanoparticles deposit on the surface and tend to decrease the surface contact angle by filling in the cavities and smoothing the surface. The nucleation site density variations with contact angle change agree with the nanofluid boiling experiments.

3.3. Bubble departure frequency

Bubble departure diameter is obtained using a relationship provided by Carey [48]:

$$D_d = \frac{1.65d^*\sigma}{g(\rho_l - \rho_v)} + \left[\frac{15.6\rho_l}{g(\rho_l - \rho_v)}\right]^{1/3}\left[\frac{\beta_d k_l(T_w - T_{sat})}{h_{fg}\rho_v}\right] \tag{54}$$

where $d^* = 6.0\times10^{-3}$ mm and $\beta_d = 6.0$. The bubble departure frequency can be obtained using the bubble growth equation and can be expressed as:

$$f = \frac{1}{\pi}Ja^2\frac{\alpha}{D_d^2} \tag{55}$$

3.4. Average heat flux and CHF calculation

The total heat transfer in one bubble ebullition cycle can be obtained by adding the five heat transfer contributions. The average heat flux at the surface can be obtained as

$$q'' = (Q_{me} + Q_{re} + Q_{tc} + Q_{mc} + Q_{nc})\cdot f\cdot N_{sd} \tag{56}$$

Over the low heat flux region, Q_{tc} and Q_{mc} are expressed using Eqs. (30) and (48) and for the high heat flux region, Q_{tc} and Q_{mc} are expressed using Eqs. (36) and (50). Q_{nc} is expressed in Eq. (43) for low to moderate heat flux while it becomes negligible over high heat flux region. Q_{me} is expressed by the radial integration of q''_{me} given by Eq. (16) and Q_{re} is expressed by Eq. (40).

Based on our model results, transient conduction is the dominant mode of heat transfer at higher superheats, accounting for nearly 70% of the total heat transfer at higher superheats while microconvection is about 10% of the total heat transfer. Microlayer evaporation accounts for less than 10% of the total heat transfer while natural convection accounts for about 60% of the total heat transfer at very low superheats. However, this percentage decreases dramatically when the superheat increases.

The critical heat flux can also be obtained by our analytical model. When the dryout fraction F exceeds a certain value, most of the surface is occupied by vapor thus retarding the liquid from the bulk pool region to flow down to wet the surface. Also, when the bubbles are too close together, they will begin to touch each other and coalesce resulting in a large vapor blanket that covers the surface. CHF is considered to occur when all the bubbles merge and the liquid cannot flow down to wet the liquid. According to Zuber [28], when

$$N_{sd}D_b^2 = 1 \tag{57}$$

static bubble interactions will occur. Under this condition, the dryout fraction F is $\pi/4$ according to Eq. (31). As such, the heat flux at a dryout fraction of $\pi/4$ is considered to be CHF.

4. Results and discussion

4.1. Average heat transfer characteristics

Rohsenow's correlation [26] is widely used to represent pool boiling as shown in Eq. (58).

$$q'' = \mu_f h_{fg}\left(\frac{g(\rho_f-\rho_v)}{\sigma}\right)^{1/2}\left[\frac{c_f(T_w-T_{sat})}{\mathrm{Pr}_f^s C_{sf} h_{fg}}\right]^3 \tag{58}$$

For water, the exponent of Pr, s is chosen as 1.0. Dimensionless factor C_{sf} accounts for the particular combination of surface and liquid characteristics. Usually C_{sf} can range from 0.0065 to 0.0215. The value 0.013 is often chosen for water–copper and water–platinum combination. Rohsenow's correlation is widely used in engineering applications since it was proposed in 1952. However, Rohsenow's model was based on analogy to forced convection and did not consider some main mechanisms, such as microlayer evaporation, transient conduction, etc., in nucleate pool boiling. Also, Rohsenow's correlation does not explain the mechanism of how C_{sf} is chosen while the value of C_{sf} can greatly affect the predicted heat flux.

Surface contact angle is an important parameter to represent surface conditions as suggested by a number of researchers [7–9,25]. In the present work, water is chosen as the base fluid. The present model calculates different heat flux characteristics at different contact angles. The predicted results of the present analytical model were compared with the results calculated by Rohsenow's correlation in Fig. 2. Researchers have reported different contact angles [7–9,14,15] in the range of 60–80° when the surface is clean while in the presence of nanofluids the contact angle is in the range of 16–45°. As can be seen in Fig. 2, the average heat flux when the contact angle equals to 60° is very close to the average heat flux calculated by the Rohsenow's correlation when C_{sf} equals to 0.0136. The heat flux at a contact angle of 70° corresponds to the heat flux when C_{sf} equals to 0.013, and the results

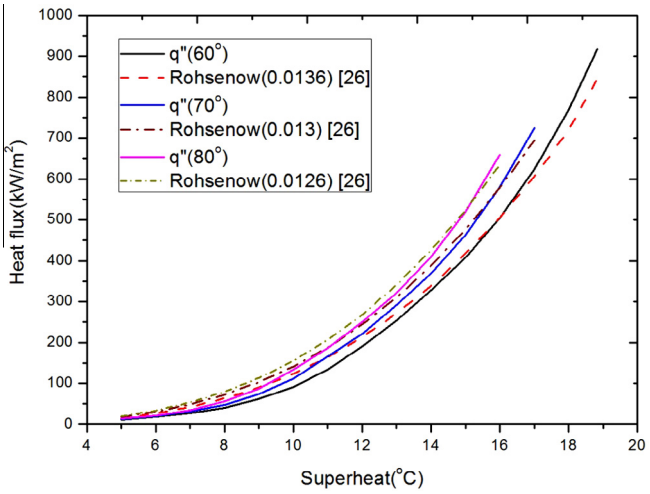

Fig. 2. Comparison of calculated average heat flux using the present analytical model in the range of contact angles from 60° to 80° with Rohsenow's correlations at different values of C_{sf}.

calculated with a C_{sf} of 0.0126 are close to the predicted results based on the present model when the contact angle is 80°. The results show that the average heat flux decreases with a decrease in the contact angle at the same surface temperature. When the superheat is 15 K, the average heat flux decreases from 521 kW/m^2 when the contact angle is 80° to 408 kW/m^2 when the contact angle is 60°. The deterioration is up to 21.6%. However, the maximum heat flux increases with a decrease in the contact angle. The maximum heat flux reaches 690 kW/m^2 when the contact angle is 80°. When the contact angle decreases to 60°, the maximum heat flux increases to 917 kW/m^2 at a superheat of 18.84 K.

Fig. 2 shows some differences between our model and Rohsenow's equation. The differences between our model and Rohsenow's correlation are as follows:

1. Even though Rohsenow's correlation is widely used in engineering applications, there is a need for a more robust result for the average heat flux. Furthermore, Rohsenow's correlation applies for clean surfaces. When it is used to estimate the heat flux, it will not be accurate. Also, Rohsenow's correlation is an empirical correlation, while our model is based on the pertinent physical mechanisms.
2. Our model establishes a relationship between the average heat flux and the surface contact angle, while Rohsenow's correlation essentially shows the average heat flux changes for different surfaces with different C_{sf}. Furthermore, it does not explain how C_{sf} is chosen and the correlation does not directly relate the average heat flux and the surface contact angle.
3. Our model was based on four heat transfer mechanisms that occur during different stages of nucleate boiling. Rohsenow's correlation is mainly based on an analogy of nucleate boiling to forced convection, which may not accurately reflect the many complicated heat transfer mechanisms during the boiling process.
4. Rohsenow's correlation is mainly based on $q'' \propto T^3$, while our model incorporates four different heat transfer mechanisms.

Based on a number of prior research works [7–9,14,15], the surface contact angle decreases after the introduction of a nanofluid instead of a regular fluid due to the deposition of nanoparticles in the boiling process as shown in Table 1. The present model is validated by comparing our results against a number of recent

experimental results. The experimental data were selected from the works of Gerardi et al. [15] and of Bang and Chang [49]. Gerardi et al. [15] reported a contact angle of 80° for boiling with pure water and 16° for boiling with nanofluids. So 80° and 16° were used in our analytical model respectively. Bang and Chang [49] did not report contact angles, so the contact angle for the base fluid water in the present model is assumed to be 60° and the contact angle for nanofluid is 30° based on previous publications [7–9,14]. The water properties are used for the cases where the contact angle is 60° and 80°, and the properties of the nanofluid are used for the cases where the contact angle is 16° and 30°. The comparisons between our analytical model and the experimental results are shown in Fig. 3. As can be seen in Fig. 3, the analytical results are very close to the experimental results.

Fig. 3 shows that the average heat flux when the contact angle is 60° is very close to the experimental results using pure water in Bang and Chang [49]. The predicted heat flux at a contact angle of 30° is very close to the experimental results with nanofluid from Bang and Chang. The pure water heat fluxes from Gerardi et al. [15] are also close to the predicted results when the contact angle is 80° and the experimental results using nanofluid are close to analytical results when the contact angle is 16°. The change in nanofluid properties had little effect on the heat transfer. That is even though the thermal conductivity increases due to the addition of the nanoparticles, the decrease in the active nucleation sites is more dominant than the property change of the boiling liquid, so the average heat flux still decreases even as the thermal properties of the liquid enhances.

The heat transfer coefficient and the Nusselt number at different wall heat fluxes are plotted and compared with the experimental results from Suriyawong et al. [17] in Fig. 4. Again, since the cited reference did not provide contact angle values, it is assumed that 80° is the contact angle for a clean surface and 45° is the contact angle for the nanofluid boiling surface. The pure water experimental results agree well with the analytical results when the contact angle is 80°, and the experimental results utilizing 0.1% nanofluid agree well with the predicted analytical results when the contact angle is 45°.

The heat transfer coefficients and Nusselt number decrease with a decrease with contact angle. When the wall heat flux is 320 kW/m^2, the heat transfer coefficient decreases from 2.47×10^4 W/m^2 K at a contact angle of 80° to 2.14×10^4 W/m^2 K at a contact angle of 45°. The heat transfer coefficient deterioration

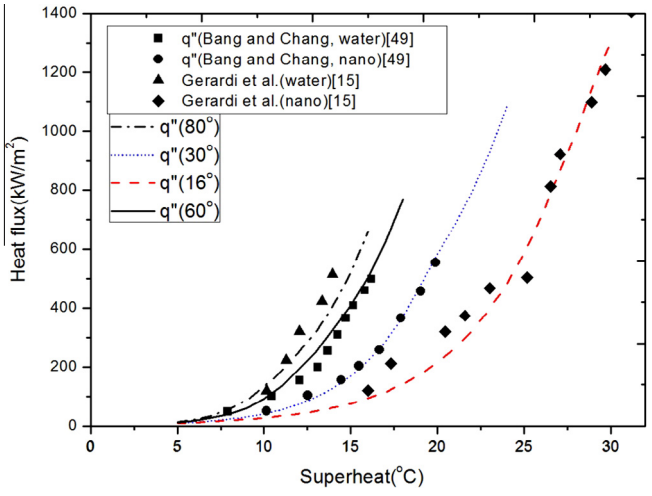

Fig. 3. Comparison of calculated average heat flux using the present analytical model with the experimental results for pure water and nanofluid boiling (experimental results from Refs. [8,49]).

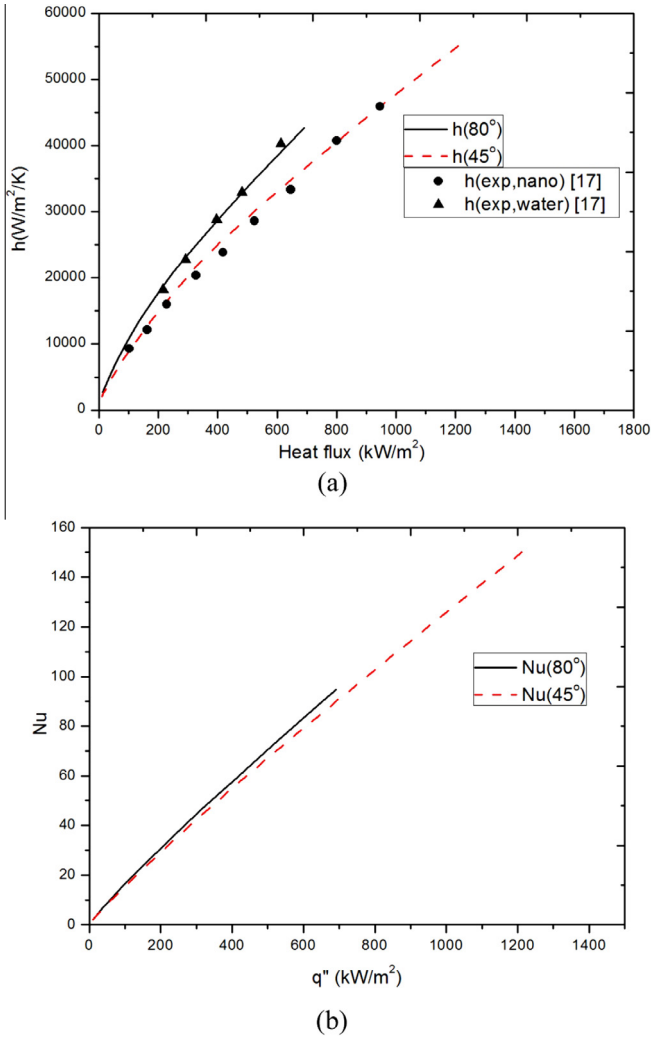

Fig. 4. Variations of (a) heat transfer coefficient and (b) Nusselt number with average wall heat flux predicted by the present analytical model for both pure water and nanofluid boiling (experiment data from Suriyawong et al. [17]).

is about 13.3% at a wall heat flux of 320 kW/m^2. The Nusselt number decreases from 47.2 to 45.1 at this wall heat flux. Although heat transfer deteriorates at the same wall heat flux, the maximum heat transfer coefficient and Nu at a smaller contact angle are higher than the heat transfer coefficient at a larger contact angle. Therefore, it appears that in nanofluid boiling, a larger maximum heat transfer coefficient and Nu can be obtained. The maximum heat transfer coefficient at a contact angle of 80° is 4.3×10^4 W/m^2 K, while the maximum heat transfer coefficient at a contact of 45° is 5.5×10^4 W/m^2 K. The Nusselt number is 94.7 and 151 respectively for these two contact angles. Our analytical results confirm these experimental trends.

4.2. CHF predictions

The critical heat flux can be enhanced in nanofluid boiling as shown by various researchers [8–15,18–20]. Many researchers suggest that when the contact angle decreases, the critical heat flux increases [7–9,14,15]. Experimental results for CHF from several researchers were compared with the CHF predicted by the present model. Different critical heat flux at different contact angles were plotted in Fig. 5 and compared with the experimental

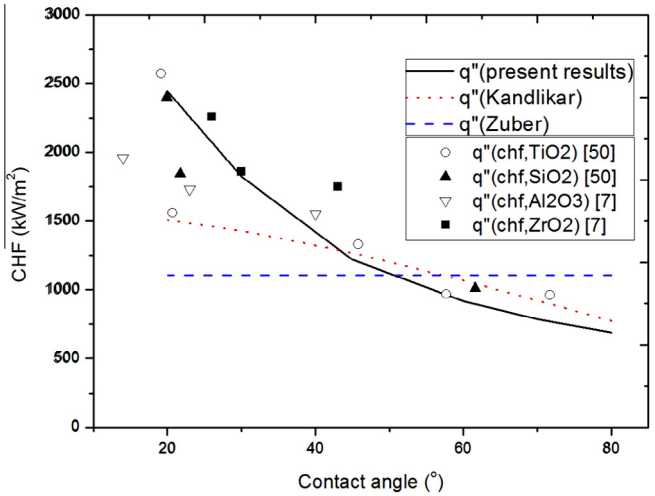

Fig. 5. Comparison of critical heat flux calculated from the present analytical model against the experimental results and classical correlations [34,36] in pure water and nanofluid boiling (experimental data from Refs. [7,50]).

results from Kim et al. [7] and Kim and Kim [50]. Kandlikar's model [36] and Zuber's correlation [34] were also plotted in Fig. 5.

Fig. 5 shows that the critical heat flux increases from 691 kW/m^2 at a contact angle of 80°, which is measured for pure water on the heating surface, to 2450 kW/m^2 at a contact angle of 20°, which is the measured value for a contact angle after the nanofluid deposition [15]. The present model predicts a higher CHF enhancement than the Kandlikar's model. The enhancement ratio is up to 3.54 if the CHF at a contact angle of 80° is chosen as the base value. Kandlikar's model predicts an enhancement ratio of 1.95 when the contact angle decreases from 80° to 20°. Zuber's model did not consider the surface conditions. The CHF predicted by Zuber's correlation is almost the same with the CHF calculated with the present model at a 53° contact angle. The enhancement ratio predicted by the present analytical model is closer to the CHF enhancement reported in the literature [12,13,20,24]. The enhancement ratio variations of the present model with a change of contact angle were plotted in Fig. 6 which shows a continuous increase of CHF with a decrease in the contact angle.

The variations of CHF with departure diameters are plotted in Fig. 7. When the contact angle is lower, the surface superheat needed for the CHF occurrence is larger, and larger bubble

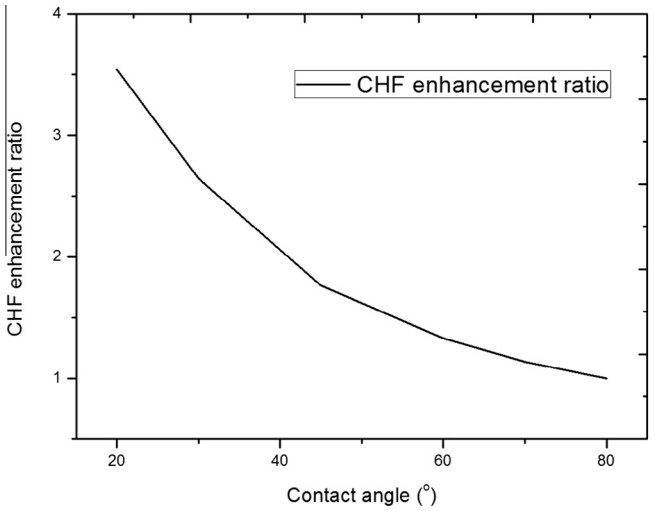

Fig. 6. Enhancement ratio variations of the critical heat flux for the present model vs. the contact angle.

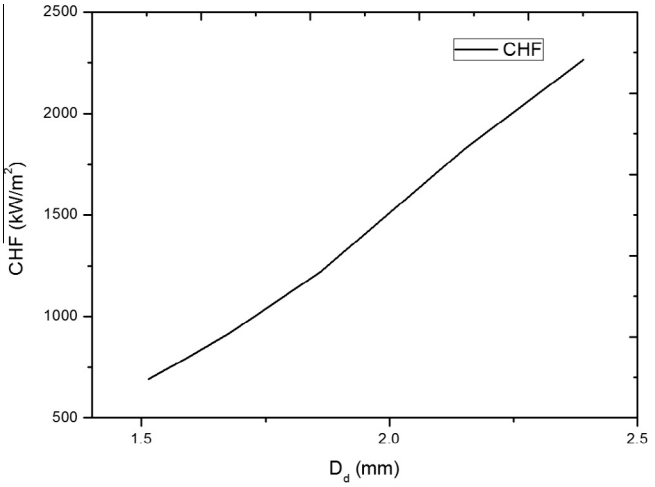

Fig. 7. Critical heat flux variations vs. the departure diameter, D_d.

diameters are needed. Larger bubble diameters and bubble departure frequencies at higher superheats result in higher heat fluxes.

5. Conclusions

In this work, a composite model is proposed to compute the average surface heat flux and the average heat flux variations with increasing superheats. The CHF was also predicted for different surface contact angles. Prior theoretical models on nucleate boiling are based on a single mechanism. However, four pertinent mechanisms affect the boiling process. Few researchers have systematically proposed a composite model analyzing these four main mechanisms. The main mechanisms in pool boiling were considered in the presented analytical model. Microlayer evaporation, transient conduction before and after bubble departs from the surface, microconvection induced by bubble growth and movement were all analyzed in the present model.

Our model has established a relationship between the average heat flux and surface contact angle. Our model has also extended the single bubble region to bubble interference region and enables quantification of the average heat flux at very high superheats. Transient conduction was found to be the main mechanism at larger superheats and natural convection accounts for a large percentage of heat transfer at very low superheats.

It was found that even though the thermal conductivity and other thermal properties were enhanced for nanofluids, the decreasing number of active nucleation sites at lower contact angles was more predominant and resulted in a decrease of the average surface heat fluxes for the same superheat. However, a larger heat transfer coefficient and Nu can be obtained for nanofluid boiling at a higher superheat. The results from our model were in good agreement with the available experimental results. Our model establishes a relationship between the average heat flux and surface contact angle leading to determination of CHF. It was also established that CHF enhancement ratio can be up to 3.54 when the surface contact angle decreases from 80° to 20°. This enhancement ratio agrees with a number of experimental results.

Conflict of interest

None declared.

Acknowledgments

This work was supported by the Science Fund for Creative Research Groups of National Natural Science Foundation of China,

Grant No. 51321002 and National Basic Research Program of China ("973" Project) Grant No. 2011CB706904. The authors acknowledge the financial support from China Scholarship Council.

References

[1] A.V. Kuznetsov, D.A. Nield, Natural convective boundary-layer flow of a nanofluid past a vertical plate, Int. J. Therm. Sci. 49 (2010) 243–247.
[2] M. Shafahi, V. Bianco, K. Vafai, O. Manca, An investigation of the thermal performance of cylindrical heat pipes using nanofluids, Int. J. Heat Mass Transfer 53 (2010) 376–383.
[3] D.A. Nield, A.V. Kuznetsov, The Cheng–Minkowycz problem for natural convective boundary-layer flow in a porous medium saturated by a nanofluid, Int. J. Heat Mass Transfer 52 (2009) 5792–5795.
[4] H. Kim, Enhancement of critical heat flux in nucleate boiling of nanofluids: a state-of-art review, Nanoscale Res. Lett. 6 (2011) 415.
[5] S.K. Das, N. Putra, W. Roetze, Pool boiling characteristics of nano-fluids, Int. J. Heat Mass Transfer 46 (2003) 851–862.
[6] J.S. Coursey, J. Kim, Nanofluid boiling: the effect of surface wettability, Int. J. Heat Fluid Flow 29 (2008) 1577–1585.
[7] S.J. Kim, I.C. Bang, J. Buongiorno, L.W. Hu, Surface wettability change during pool boiling of nanofluids and its effect on critical heat flux, Int. J. Heat Mass Transfer 50 (2007) 4105–4116.
[8] Z. Shahmoradi, N. Etesami, M.n.N. Esfahany, Pool boiling characteristics of nanofluid on flat plate based on heater surface analysis, Int. Commun. Heat Mass Transfer 47 (2013) 113–120.
[9] J.Y. Jung, E.S. Kim, Y. Nam, Y.T. Kang, The study on the critical heat flux and pool boiling heat transfer coefficient of binary nanofluids (H_2O/LiBr + Al_2O_3), Int. J. Refrig. 36 (2013) 1056–1061.
[10] D.M. Vazquez, R. Kumar, Surface effects of ribbon heaters on critical heat flux in nanofluid pool boiling, Int. Commun. Heat Mass Transfer 41 (2013) 1–9.
[11] J.Y. Jung, E.S. Kim, Y.T. Kang, Stabilizer effect on CHF and boiling heat transfer coefficient of alumina/water nanofluids, Int. J. Heat Mass Transfer 55 (2012) 1941–1946.
[12] R.N. Hegde, S.S. Rao, R.P. Reddy, Experimental studies on CHF enhancement in pool boiling with CuO–water nanofluid, Int. J. Heat Mass Transfer 48 (2012) 1031–1041.
[13] M. Kole, T.K. Dey, Investigations on the pool boiling heat transfer and critical heat flux of ZnO–ethylene glycol nanofluids, Appl. Therm. Eng. 37 (2012) 112–119.
[14] A. Bolukbasi, D. Ciloglu, Pool boiling heat transfer characteristics of vertical cylinder quenched by SiO_2–water nanofluids, Int. J. Therm. Sci. 50 (6) (2011) 1013–1021.
[15] C. Gerardi, J. Buongiorno, L.W. Hu, T. McKrell, Infrared thermometry study of nanofluid pool boiling phenomena, Nanoscale Res. Lett. 6 (2011) 232–248.
[16] D. Wen, M. Corr, X. Hu, G. Lin, Boiling heat transfer of nanofluids: the effect of heating surface modification, Int. J. Therm. Sci. 50 (4) (2011) 480–485.
[17] A. Suriyawong, S. Wongwises, Nucleate pool boiling heat transfer characteristics of TiO_2–water nanofluids at very low concentrations, Exp. Therm. Fluid Sci. 34 (2010) 992–999.
[18] S.M. Kwark, R. Kumar, G. Moreno, J. Yoo, S.M. You, Pool boiling characteristics of low concentration nanofluids, Int. J. Heat Mass Transfer 53 (2010) 972–981.
[19] Z. Liu, J. Xiong, R. Bao, Boiling heat transfer characteristics of nanofluids in a flat heat pipe evaporator with micro-grooved heating surface, Int. J. Multiphase Flow 33 (2007) 1284–1295.
[20] S.M. You, J.H. Kim, K.H. Kim, Effect of nanoparticles on critical heat flux of water in pool boiling heat transfer, Appl. Phys. Lett. 83 (2003) 3374–3376.
[21] D. Wen, Y. Ding, Experimental investigation into the pool boiling heat transfer of aqueous based γ-alumina nanofluids, J. Nanoparticle Res. 7 (2005) 265–274.
[22] H. Kim, J. Kim, M. Kim, Experimental study on CHF characteristics of water–TiO_2 nano-fluids, Nucl. Eng. Technol. 38 (1) (2006) 61–68.
[23] O. Ahmed, M.S. Hamed, Experimental investigation of the effect of particle deposition on pool boiling of nanofluids, Int. J. Heat Mass Transfer 55 (13–14) (2012) 3423–3436.
[24] T. Okawa, M. Takamura, T. Kamiya, Boiling time effect on CHF enhancement in pool boiling of nanofluids, Int. J. Heat Mass Transfer 55 (9–10) (2012) 2719–2725.
[25] C.H. Wang, V.K. Dhir, Effect of surface wettability on active nucleation site density during pool boiling of water on a vertical surface, ASME J. Heat Transfer 115 (1993) 659–669.
[26] W.M. Rosenhow, A method of correlating heat transfer data for surface boiling of liquids, Trans. ASME J. Heat Transfer 4 (1952) 969–975.
[27] C.L. Tien, A Hydrodynamic model for nucleate pool boiling, Int. J. Heat Mass Transfer 5 (1962) 540–553.
[28] N. Zuber, Nucleate boiling the region of isolated bubbles and the similarity with natural convection, Int. J. Heat Mass Transfer 6 (1963) 53–78.
[29] H.K. Forster, R. Greif, Heat transfer to a boiling liquid-mechanisms and correlations, ASME J. Heat Transfer 81 (1959) 45.
[30] C.Y. Han, P. Griffith, The mechanism of heat transfer in nucleate pool boiling, Int. J. Heat Mass Transfer 8 (1965) 887–914.
[31] B.B. Mikic, W.M. Rohsenow, A new correlation of pool boiling data including the effect of heating surface characteristics, ASME J. Heat Transfer 91 (1969) 245–250.
[32] R.L. Judd, K.S. Hwang, A comprehensive model for nucleate pool boiling heat transfer including microlayer evaporation, ASME J. Heat Transfer 98 (1976) 623–629.
[33] R.J. Benjamin, A.R. Balakrishnan, Nucleate pooling heat transfer of pure liquids at low to moderate heat fluxes, Int. J. Heat Mass Transfer 39 (1996) 2495–2504.
[34] N. Zuber, On the stability of boiling heat transfer, ASME J. Heat Transfer 80 (2) (1958) 711–720.
[35] Y. Haramura, Y. Katto, New hydrodynamic model of critical heat flux applicable widely to both pool and forced convection boiling on submerged bodies in saturated liquids, Int. J. Heat Mass Transfer 26 (1983) 379–399.
[36] S.G. Kandlikar, A theoretical model to predict pool boiling CHF incorporating effects of contact angle and orientation, ASME J. Heat Transfer 123 (2001) 1071–1079.
[37] K. Khanafer, K. Vafai, A critical synthesis of thermophysical characteristics of nanofluids, Int. J. Heat Mass Transfer 54 (2011) 4410–4428.
[38] G. Batchelor, The effect of Brownian motion on the bulk stress in a suspension of spherical particles, J. Fluid Mech. 83 (1977) 97–117.
[39] G. Son, V.K. Dhir, N. Ramanujapu, Dynamics and heat transfer associated with a single bubble during nucleate boiling on a horizontal surface, ASME J. Heat Transfer 121 (1999) 623–631.
[40] J.L. Bi, X.P. Lin, D.M. Christopher, Effects of bubble coalescence dynamics on heat flux distributions under bubbles, AICHE J. 59 (2013) 1735–1745.
[41] C. Gerardi, J. Buongiorno, L. Hu, T. McKrell, Study of bubble growth in water pool boiling through synchronized, infrared thermometry and high-speed video, Int. J. Heat Mass Transfer 53 (2010) 4185–4192.
[42] S. Moghaddam, K. Kiger, Physical mechanisms of heat transfer during single bubble nucleate boiling of FC-72 under saturation conditions-I, Exp. Invest. Int. J. Heat Mass Transfer 52 (2009) 1284–1294.
[43] S. Moghaddam, K. Kiger, Physical mechanisms of heat transfer during single bubble nucleate boiling of FC-72 under saturation conditions-II, Theor. Anal. Int. J. Heat Mass Transfer 52 (2009) 1295–1303.
[44] J.L. Bi, X.P. Lin, D.M. Christopher, X.F. Li, Analysis of coalescence phenomena on microheaters at two surface superheats, Int. J. Heat Mass Transfer 67 (2013) 798–809.
[45] J.L. Bi, D.M. Christopher, X.P. Lin, X.F. Li, Effects of nucleation site arrangement and spacing on bubble coalescence characteristics, Exp. Therm. Fluid Sci. 52 (2014) 116–127.
[46] H.K. Forster, N. Zuber, Dynamic of vapor bubbles and boiling heat transfer, AIChE J. 1 (1955) 531–539.
[47] T. Hibiki, M. Ishii, Active nucleation site density in boiling systems, Int. J. Heat Mass Transfer 46 (2003) 2587–2601.
[48] V.P. Carey, Liquid Vapor Phase-transition Phenomena, Hemisphere, New York, 1992. pp. 207.
[49] I.C. Bang, S.H. Chang, Boiling heat transfer performance and phenomena of Al_2O_3–water nano-fluids from a plain surface in a pool, Int. J. Heat Mass Transfer 48 (2005) 2407–2419.
[50] H.D. Kim, M.H. Kim, Effect of nanoparticle deposition on capillary wicking that influences the critical heat flux in nanofluids, Appl. Phys. Lett. 91 (2007) 014104.